

A 3D Bioprinted Nanoengineered Hydrogel with Photoactivated Drug Delivery for Tumor Apoptosis and Simultaneous Bone Regeneration via Macrophage Immunomodulation

Sayan Deb Dutta, Keya Ganguly, Jin Hexiu, Aayushi Randhawa, Md Moniruzzaman,* and Ki-Taek Lim*

One of the significant challenges in bone tissue engineering (BTE) is the healing of traumatic tissue defects owing to the recruitment of local infection and delayed angiogenesis. Herein, a 3D printable multi-functional hydrogel composing polyphenolic carbon quantum dots (CQDs, $100 \mu\text{g mL}^{-1}$) and gelatin methacryloyl (GelMA, 12 wt%) is reported for robust angiogenesis, bone regeneration and anti-tumor therapy. The CQDs are synthesized from a plant-inspired bioactive molecule, 1, 3, 5-trihydroxybenzene. The 3D printed GelMA-CQDs hydrogels display typical shear-thinning behavior with excellent printability. The fabricated hydrogel displayed M2 polarization of macrophage (Raw 264.7) cells via enhancing anti-inflammatory genes (e.g., *IL-4* and *IL10*), and induced angiogenesis and osteogenesis of human bone mesenchymal stem cells (hBMSCs). The bioprinted hBMSCs are able to produce vessel-like structures after 14 d of incubation. Furthermore, the 3D printed hydrogel scaffolds also show remarkable near infra-red (NIR) responsive properties under 808 nm NIR light (1.0 W cm^{-2}) irradiation with controlled release of antitumor drugs ($\approx 49\%$) at pH 6.5, and thereby killing the osteosarcoma cells. Therefore, it is anticipated that the tissue regeneration and healing ability with therapeutic potential of the GelMA-CQDs scaffolds may provide a promising alternative for traumatic tissue regeneration via augmenting angiogenesis and accelerated immunomodulation.

remains challenging in the clinic. The conventional strategy for tissue regeneration of exogenous or endogenous tissue requires longer time and the healing rate is relatively slow.^[1] One of the fundamental processes of tissue regeneration is rapid proliferation and migration of cells toward the damaged tissue. Immune cells play vital role in tissue healing via boosting the proliferation of stem cells and neo-angiogenesis. Among the various immune-associated cells, macrophages play a considerable role in the regeneration of damaged tissue via the secretion of inflammatory factors.^[1a, 2] The macrophages are derived from monocyte cells which are originally the myeloid progenitor cells of the adult bone marrow.^[2] Based on the nature and function, the macrophage can be subdivided into two main types: M1 and M2 type. The M1 or pro-inflammatory macrophages are mainly involved in necrosis, microbe removal, tumor clearance, excessive fibrosis, and anti-healing functions via secretion of pro-inflammatory cytokines and chemokines (e.g., $\text{IL-1}\beta^{\text{high}}$, $\text{IL-6}^{\text{high}}$, and $\text{TNF}\alpha^{\text{high}}$, $\text{IL-12}^{\text{high}}$, $\text{IL-23}^{\text{high}}$, and $\text{IL-10}^{\text{low}}$). The M1

1. Introduction

Regeneration of damage tissue, such as skin or bone due to accidental injury, trauma, bacterial infection or inflammation


phenotype typically metabolize arginine (Arg) and produce high level of inducible nitric oxide synthase (iNOS or NOS2), followed by secretion of toxic reactive oxygen species (ROS), and nitric oxide (NO). Besides, the M2 macrophages are “alternatively

S. D. Dutta, K. Ganguly, A. Randhawa, K.-T. Lim
Department of Biosystems Engineering
College of Agriculture and Life Sciences
Kangwon National University
Chuncheon 24341, Republic of Korea
E-mail: ktlim@kangwon.ac.kr

J. Hexiu
Department of Oral and Maxillofacial Surgery
Capital Medical University
Beijing China

A. Randhawa, K.-T. Lim
Interdisciplinary Program in Smart Agriculture
Kangwon National University
Chuncheon 100069, Republic of Korea

M. Moniruzzaman
Department of Chemical and Biological Engineering
Gachon University
Seongnam 1342, Republic of Korea
E-mail: mani57chem@gachon.ac.kr

 The ORCID identification number(s) for the author(s) of this article can be found under <https://doi.org/10.1002/mabi.202300096>

DOI: 10.1002/mabi.202300096

activated" macrophages which mainly activated through various intracellular (IL-4 or IL-10) or extracellular signals (nanoparticles or proteins)^[3] and secrete anti-inflammatory factors (e.g., IL-4^{high}, IL-13^{high}, IL-10^{high}, IL-6^{low}, IL-12^{low}, and IL23^{low}). The M2 macrophages are mainly associated with tissue healing and regeneration, such as osteogenesis, angiogenesis, melanogenesis, and among others.^[2,4] Thus, a balance between the M1 and M2 macrophage dictates the fate of tissue regeneration or inflammation. Biomimetic scaffolds can be used to manipulate the phenotypic plasticity of the macrophages. The scaffold's topology, surface function group, chemical composition, wettability, self-assembly, and surface roughness chiefly regulates the macrophage fate.^[5] Therefore, a significant shift from pro-inflammatory to anti-inflammatory response may affect the alteration of IL-10, transforming growth factor- β (TGF- β), bone morphogenic protein-2 (BMP-2), vascular endothelial growth factor (VEGF), fibroblast growth factor (FGF) secretion, respectively.^[1a, 5b]

Bone is a highly specialized and complex tissue which is mainly characterized by the rigidity and harness, and the harbor for osteogenic and hematopoietic progenitor cells. Several pathological conditions including infection, swelling, fractures, arthritis, osteoporosis, osteonecrosis, and osteosarcoma (= bone cancer) may damage the bone tissue. Among them, the effective strategy against fracture healing and osteosarcoma remain challenging in the clinic owing to the lack of suitable orthopedic/theranostic implants.^[6] Although several advances have been encountered in past few years for treating bone defects;^[7] however, most of the orthopedic implants failed to demonstrate the quality control and in vivo safety concerns, making it inappropriate for clinical trial.^[8] For example, growth factor-loaded orthopedic implants exert serious health issues including transplantation risks (e.g., host rejection), faulty immune response, immune suppression, and organ damage. To some extent, the allogeneic transplants may cause toxicity and chronic infection which ultimately lead to bone tumor formation.^[1a, 9] To address this issue, a "multi-functional immunomodulatory" scaffold combining all the necessary functions is highly desirable which could surpass the existing barrier in bone healing/therapy. During fracture healing, the monocyte cells infiltrated to the wound site and repair the damaged tissue via promoting osteoblast migration through the secretion of various anti-inflammatory cytokines and chemokines (M2 phenotype). The M2 macrophages also stimulate the endothelial and osteoblast cells to secrete VEGF and BMP-2 via paracrine signaling which promote the neo-angiogenesis and osteogenesis.^[10] Recent studies indicate that angiogenesis is one of the crucial factor during bone regeneration, suggesting that there must a molecular cross-talk between osteoblast and endothelial cells with immune cells.^[11]

Nowadays, researchers are developing multi-functional bioactive scaffolds through additive manufacturing (AM) technology via tuning the surface chemistry,^[12] incorporation of bioactive coating,^[13] drugs,^[14] nanomaterials,^[15] and a variety of cells^[16] to facilitate osteo-immunity. Among them, gelatin methacryloyl (GelMA)-based bioprinted hydrogels have been gained enormous attention owing to their exceptional bioactivity, cytocompatibility, and mechanical property.^[17] Also, various kinds of metal-based nano-hydroxyapatite and their composites have been shown to stimulate bone formation (Table S1, Supporting Information)

through M2 macrophage polarization via extracellular receptor kinase (ERK) or Janus kinase/signal transducer and activator of transcription (JAK/STAT) signaling pathway.^[18] Li et al. reported the use of lithium-doped HAp/heparin hydrogel loaded with transforming growth factor- β (TGF- β) for M2 macrophage polarization and robust bone regeneration. Recently, carbon based bioactive molecules, such as carbon quantum dots (CQDs), carbon nanotubes (CNTs) and MXene ($M_{n+1}AX_n$)-based composites has been shown to have immunomodulatory properties.^[19] These materials are extensively used as biomaterials owing to their nano-dimensional size, excellent near-infrared (NIR) responsive property, and tunable surface functionality with superior biocompatibility.^[19a] However, the role of these carbon-based materials in dynamic immunomodulation and bone regeneration in a 3D printed hydrogel is still unknown. The CQDs with tunable surface chemistry may also have tremendous application in drug delivery for treating several cancers and malignant carcinomas.^[20] Thus, development of a multifaceted hydrogel integrating all the above-mentioned feature is highly desirable for traumatic tissue healing and regeneration.

In this study, we reported a 3D printable "multi-functional" nanohybrid scaffold composing gelatin methacryloyl (GelMA) and polyphenolic carbon quantum dots (CQDs) for endogenous (bone) tissue repair and therapy (Scheme 1). The CQDs were synthesized from a plant-inspired bioactive molecule, phloroglucinol (1, 3, 5-trihydroxybenzene) via facile wet chemistry method. In an in vivo bone defect model, the fabricated GelMA-CQD scaffold was able to accelerate the bone healing after 8 weeks without any supplement of drugs/growth factors. The as-printed scaffold was also able to promote osteogenesis of human bone marrow-derived mesenchymal stem cells (hBMSCs) through immune cross-talk with macrophages in a 2D and 3D culture model. The outstanding near infra-red (NIR)-responsive property of the CQDs was utilized for in vitro osteosarcoma therapy via controlled delivery of doxorubicin (Dox). Taken together, our developed scaffold holds many promises towards multi-modal tissue regeneration for clinical practice, especially for treating malignant bone tumors and restoration of bone matrix.

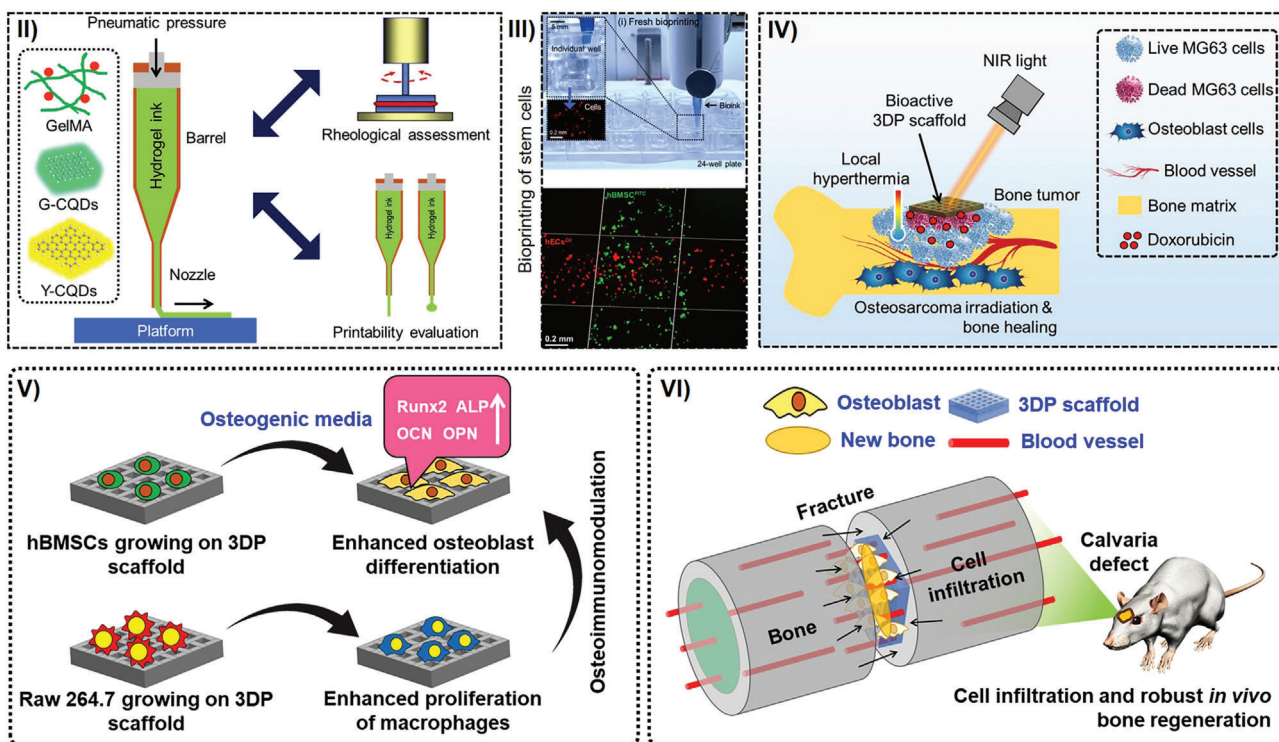
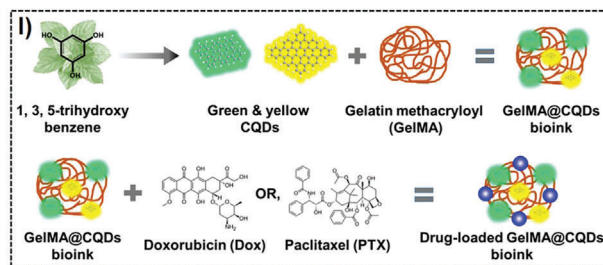
2. Results and Discussion

2.1. Physicochemical Properties of the Hydrogel Inks

The hydrogel inks were prepared using GelMA and CQDs under natural atmospheric conditions. The morphological, structural, and optical properties of the CQDs were evaluated using various microscopic and spectrometric techniques. The results are described in Figures S1–S5, (Supporting Information). For printable ink fabrication, predetermined amount (100 $\mu\text{g mL}^{-1}$) of G-CQD and Y-CQD were blended with 12 wt% GelMA solution (in 1 \times PBS), followed by addition of LAP photoinitiator (0.25%). After that, the fabricated hydrogel inks were transferred to a clean glass vial and irradiated with 365 nm UV light for 60 s. The concentration of CQDs was used as reported in our previous study.^[21] The structural property of the pure GelMA and its composite hydrogel scaffolds was evaluated using FE-SEM and the results are displayed in Figure S6 (Supporting Information). The freeze-dried GelMA and GelMA-CQD scaffold showed comparable microporous morphologies with unique porosity (Figure S6a,

MULTIFUNCTIONAL NANOENGINEERED BIOINK

- ✓ Excellent printability
- ✓ Rheological robustness
- ✓ Self-glowing
- ✓ Immunomodulatory
- ✓ Osteomodulatory
- ✓ Near infra-Red responsive
- ✓ Photo-activated delivery
- ✓ Therapeutic effects



Scheme 1. Schematic illustration of the proposed mechanism of tissue repair and regeneration by the polyphenolic CQDs-incorporated hybrid scaffold.

Supporting Information). Notably, the addition of G-CQDs and Y-CQDs significantly ($**p < 0.01$) increased the pore size compared to the pure GelMA. The average pore size of the GelMA, GelMA-G, and GelMA-Y scaffolds was calculated to be $90\text{--}155 \pm 25 \mu\text{m}$, $122\text{--}320 \pm 60 \mu\text{m}$, and $230\text{--}400 \pm 56 \mu\text{m}$, respectively (Figure S6b, Supporting Information). The porosity of GelMA scaffold has great influence on stem cells proliferation and differentiation. In particular, smaller pores ($<50 \mu\text{m}$) may induce higher osteogenesis, while larger pores ($>200 \mu\text{m}$) facilitated greater proliferation and metabolic enhancement owing to the higher availability of soluble nutrients and superior oxygen diffusion.^[17a, 22] According to prior findings, the rough and flaky pure structures of the GelMA-CQD composites made with the G- and Y-CQDs (GelMA-G and GelMA-Y) were comparable to those of the pure GelMA scaffold.^[19a] The GelMA-CQD scaffold's flaky and macroporous shape may increase swelling effectiveness and promote cell infiltration and proliferation for wound healing.^[23] The swelling behavior of the fabricated scaffolds was examined in the presence of $1 \times \text{PBS}$ at ambient temperature. One of the most important characteristics of hydrogel composites utilized in biological applications is their swelling behavior.^[16,24]

Swelling performance indirectly discloses the structural characteristics and mechanical stiffness of medical implants and is closely correlated with the rehydration capability and durability of the structures.^[23a] As shown in Figure S6c (Supporting Information), the GelMA-CQDs scaffold exhibited higher degree of swelling compared to the pure GelMA, indicating that the GelMA-CQDs scaffolds had greater hydration property. Thus, the freeze-dried GelMA scaffold proved advantageous for bone tissue regeneration because it successfully retains the moisture of the surroundings.^[25] As anticipated, the GelMA-CQD composite hydrogels had greater swelling properties than pure GelMA. The ability for hydrogels to expand is substantially influenced by the presence of hydrophilic --OH groups, the degree of crosslinking, and crystallinity.^[26] After 50 h of incubation, the swelling efficiencies of the GelMA-G and GelMA-Y composite hydrogels were much greater than those of the pure GelMA scaffold ($\approx 218\%$). The larger pores and numerous phenolic --OH groups of the polyphenolic CQDs in the GelMA-CQD composite hydrogels, which encouraged the formation of hydrogen bonds between the CQDs and GelMA scaffold, were attributed to the GelMA-CQD composite hydrogels' superior swelling potential

compared to that of the pure GelMA. Because there were more hydrophilic -OH groups accessible in the Y-CQDs than in the G-CQDs, the GelMA-Y composite hydrogel could absorb more water than the GelMA-G composite hydrogel. Additionally, the GelMA-Y composite hydrogel surpassed the GelMA-G composite hydrogel in terms of swelling behavior, expansion ratio, and solid characteristics.^[27] In light of this, we predicted that the developed GelMA-CQD hydrogel would exhibit great swelling effectiveness, unique porosity, and provide excellent spot for cell proliferation, making them beneficial as ideal material for bone tissue engineering.^[28]

2.2. Viscoelasticity and Bioprinting Properties

The viscoelastic nature and flow behavior of the composite hydrogel inks were evaluated using a rotational rheometer. Rheology is an important parameter for testing the bioinks quality for 3D printing application. **Figure 1a** depicts an overview of the characterization procedure of the developed bioinks. The bioinks were characterized through frequency (ω) sweep (0.1 to 100 Rad s^{-1}) with 1% strain rate at 25 °C. The shear moduli, for example, storage modulus (G') and loss modulus (G'') were calculated and the result is displayed in **Figure 1b**. We examined the G' and G'' values of the pure GelMA and GelMA-CQD bioinks. In comparison to pure GelMA, the G' values of the GelMA-CQDs samples increased more rapidly. At 100 Rad s^{-1} , the G' values of the GelMA-G (622 Pa) and GelMA-Y (1066 Pa) bioinks were greater than those of pure GelMA (430 Pa). The G'' values for the GelMA, GelMA-G, and GelMA-Y were calculated to be 110 Pa, 206 Pa, and 638 Pa, respectively. This was also reflected in the flow curve of the bioinks. The flow behavior of the bioinks was measured in terms of viscosity (η) versus varying shear rate ($\dot{\gamma} = 0.1$ to 100 s^{-1}). As shown in **Figure 1c**, all the fabricated bioinks exhibited shear-dependent viscosity change within the measured shear range. The bioinks displayed higher viscosity at low shear rate ($\dot{\gamma} = 0.1$ s^{-1}), followed by a sharp decrease at high shear rate ($\dot{\gamma} = 100$ s^{-1}), respectively. This indicates the typical shear-thinning nature of a printable bioink.^[29] The low curve was further fitted to the Herschel-Bulkley model to determine the value of shear-thinning index (n). The value of n for GelMA, GelMA-G, and GelMA-Y were calculated to be 0.824 ($R^2 = 0.999$), 0.667 ($R^2 = 0.998$), and 0.516 ($R^2 = 0.999$), respectively. Typically, an ideal bioink having $n < 1$ is considered as shear-thinning material, which is crucial for 3D printing and bioprinting applications.^[30] Next, we evaluated the thixotropic behavior to understand the recovery potential of the fabricated hydrogel inks. As indicated in **Figure S7** (Supporting Information), the GelMA-CQDs hydrogel inks displayed higher recovery potential compared to pure GelMA after recovery from high shear stress (100 s^{-1}). This could be due to the strong interaction of the CQDs with the GelMA matrix, which contributed to the superior elastic recovery of the GelMA-CQDs. Taken together, our results indicated that the developed GelMA-CQD bioinks were highly shear-thinning with superior recovery strength and could be used as a printable biomaterial for tissue engineering application.

Next, we evaluated the printing performance of the fabricated bioinks in vitro. The GelMA-Y hydrogel ink was chosen for 3D printing and bioprinting evaluation owing to its excellent vis-

coelastic nature and mechanical stability. **Figure 1d-i** demonstrates the effect of printing speed and pressure on the extrudability of the GelMA-Y bioink. Prior to 3D printing, a CAD model (20 × 20 × 5 mm) was constructed using the SolidWorks program and sliced using the open source software. The GelMA-Y bioink was carefully loaded onto the printing barrel and chilled at 4 °C for 30 min. After 30 min, the 3D printing was conducted keeping the print-bed temperature at 4–8 °C. Next, the printed constructs were photo-crosslinked using 365 nm UV light for 60 s and tested for printability. As shown in **Figure 1d-ii**, the printing speed and pressure profoundly affected the filament diameter and printability factor. The optimum printing pressure and speed for GelMA-Y bioink were measured to be 65 kPa and 4.5 m s^{-1} , respectively. A summary of the printing parameter is given in **Figure 1d-iii**. We tested the printing performance of the GelMA-Y hydrogel using a square and hexagonal infill pattern and after UV crosslinking the printed structures retained the shape of the CAD model (**Figure 1e**). Owing to the unique fluorescence property of the Y-CQD, the printed hydrogel appeared to be yellow color under 561 nm excitation laser. However, the hydrogel exhibited weak emission at 405 nm and 488 nm excitations. The digital micrograph with a corresponding macroscopic image of the printed construct is given in **Figure 1f**. Being a part of natural ECM, the gelatin and its composite bioinks were safe for encapsulating cells. Studies have shown that 3D bioprinted GelMA hydrogel exhibited greater visibility of encapsulated cells than other commercial bioinks.^[31] In accordance with previous reports and the exceptional biocompatibility of the GelMA-CQD hydrogel, we have chosen it for bioprinting of dual-cell constructs. For this, the hECs and hBMSCs (4 × 10⁴ each) were labeled with Dil (50 × 10⁻⁶ M, Sigma-Aldrich, USA) or FITC (1 μg mL⁻¹, Sigma-Aldrich, USA) for 30 min and mixed with 3 mL of GelMA-Y pre-gel solution. The cell-encapsulated bioink was then chilled for 5–10 min, and quickly bioprinted onto a 24-well plate (**Figure 1g-i**). The cells were then visualized using an FL microscope to check the homogeneity. The dual cell-laden constructs were then incubated with suitable growth media (first 24 h supplemented with DMEM/F12 media, and then replaced with Opti-MEM media supplemented with 100 ng mL⁻¹ VEGF) and cultured for 14 d. As shown in **Figure 1g-ii**, the cells were mostly centered towards the printed strands at day 3. Interestingly, the cells covered the whole area of the hydrogel strand after 7 d of culture (**Figure 1g-iii**). Moreover, the hEC^{Dil} tends to form vessel-like structure in cross-section of the hydrogel after 14 d of culture. The hBMSC^{FITC} were found intermingled with hEC^{Dil} vessel, which suggest that the developed bioink is capable of inducing the angiogenesis. None of the cells were found toxic to the GelMA-CQD bioink during 14 d of incubation.

Mechanical stability of hydrogel scaffold is an important factor for biomedical application, especially for bone tissue engineering.^[17a,17b] Before conducting the in vitro experiments, we tested the mechanical stability of the GelMA-Y hydrogels in DMEM media up to 14 d and the results are depicted in **Figure S8** (Supporting Information). Apart from outstanding bioprintability and biocompatibility, the GelMA-Y hydrogel exhibited excellent mechanical strength with an elastic modulus of $\approx 34.6 \pm 0.87$ kPa at day 0. After immersing in DMEM for 7 and 14 d, we observed a decrease in the compressive strength with gradual increase in elastic modulus, meaning that the hydrogel tend to behave like

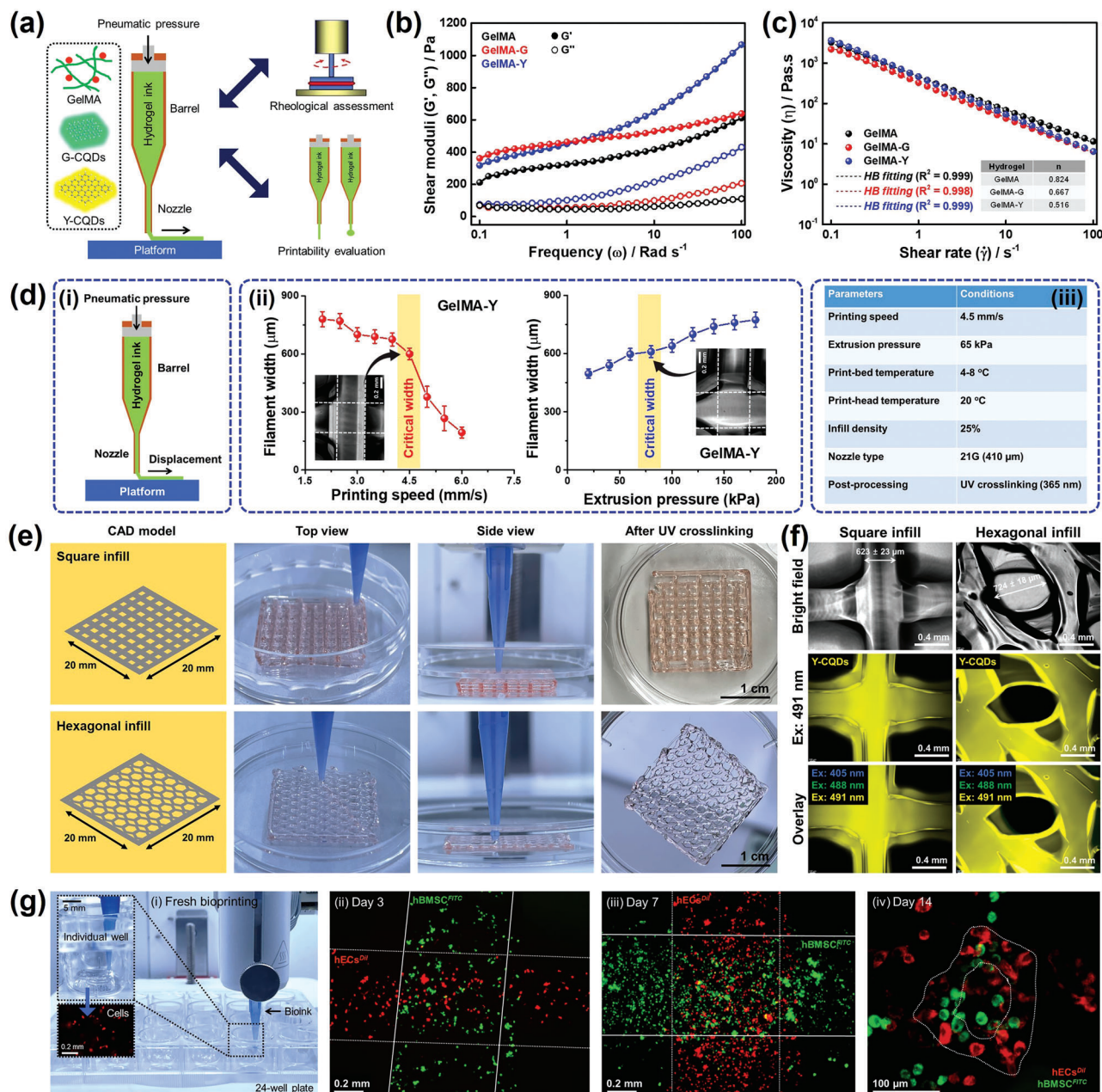


Figure 1. Optimization of the GelMA-CQDs bioinks. a) Schematic diagram of the bioink formulation and optimization strategy. b) The shear moduli (G' and G'') of the fabricated GelMA, GelMA-G, and GelMA-Y bioinks within 0.1 to 100 Rad s^{-1} range. c) Viscosity (η) as a function of shear rate ($\dot{\gamma}$) of the pure GelMA, GelMA-G, and GelMA-Y bioinks within 0.1 to 100 s^{-1} . d) optimization of the extrusion speed and printing pressure on filament formation with corresponding quantification data. e) The optimized printing parameter for the GelMA-Y bioink. Representative digital photographs and microscopic images of the 3D printed GelMA-Y hydrogels with varying infill configuration. f) Representative FL microscopy images of hEC^{DII} (red) and hBMSC^{FITC} (green) after 14 d of culture in a bioprinted construct composing GelMA-Y. Scale bar: 100 μm , 0.2 mm, and 0.4 mm.

a soft and elastic gel. The elastic modulus at day 7 and 14 was calculated to be $\approx 64.2 \pm 1.42$ and $\approx 71.6 \pm 0.74$ kPa, respectively. The GelMA-CQD-based soft hydrogel is ideal for bone marrow replacement therapy.^[17b] Taken together, we anticipated that the developed GelMA-Y bioink is superior among the various formulations, and thus suitable for soft tissue engineering applications.

2.3. In Vitro Drug Delivery and NIR-Triggered Antiosteosarcoma Therapy

Treatment of malignant bone tumor remains challenge owing to the rapid growth and metastasis of the tumor tissue.^[32] Apart from conventional therapy, the NIR-based nanotheranostic platform has gained significant attention nowadays.^[33] In this study,

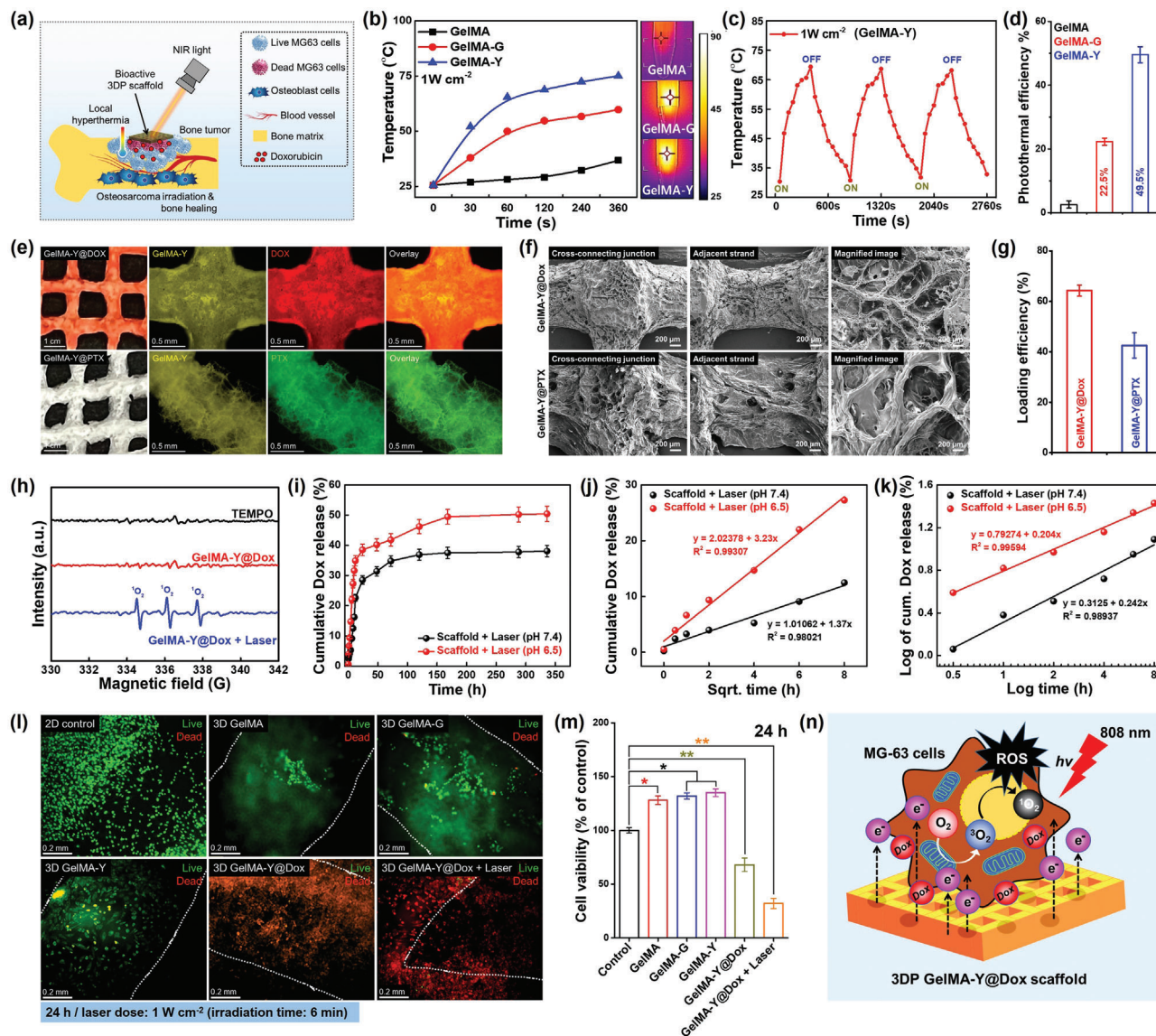


Figure 2. In vitro anti-osteosarcoma effect of the engineered GelMA-Y scaffold. a) Schematic diagram of the NIR-responsiveness of the fabricated scaffolds. b) Temperature profile as a function of time upon irradiation with 808 nm NIR laser (1 W cm⁻²). The corresponding thermal images are shown for demonstration purpose. c) Temperature stability of the GelMA-Y hydrogels after three on/off cycles under 808 nm NIR light irradiation. d) The photothermal conversion efficiency (PCE) of the developed hydrogels. e, f) Representative digital, fluorescent, and ultrastructural images of the drug loaded 3DP scaffolds. g) The drug loading efficiency of the GelMA-Y scaffold. h) EPR spectra of the pure TEMPO, GelMA-Y@Dox, and laser-treated GelMA-Y@Dox showing the presence of singlet oxygen (¹O₂) peaks. i–k) Representative Dox release study in various pH buffer (pH 6.5 and 7.4) with or without NIR light irradiation. Cumulative Dox release fitting data to Higuchi and Korsmeyer-Peppas kinetics model at 37 °C. l, m) Cytotoxicity evaluation of the MG-63 cells after irradiation with 808 nm NIR laser. Representative FL microscopy images of the MG-63 cells showing the presence of live (green) and dead (red) cells after 808 nm NIR light treatment. The cell viability was assessed using WST-8 assay. n) A hypothetical drawing of NIR-triggered hypothermia and ROS-induced bone tumor irradiation. Scale bar: 20 μm, 200 μm, and 0.2 mm. Data are reported as mean ± s.d. (n = 3), statistical significance at *p < 0.05 and **p < 0.01.

the bioactive CQDs were utilized as a photothermal source material for drug delivery and subsequent osteosarcoma therapy. **Figure 2a** depicts an overview of the NIR-triggered drug release and phototherapy for osteosarcoma therapy. The photothermal performance of the GelMA-CQDs hydrogel was evaluated using an 808 nm NIR light with a power density of 1.0 W cm⁻², respectively. As shown in **Figure 2b**, the hydrogel temperature was rapidly increased from 25 °C to 75 °C within 6 min of irradiation.

The pure GelMA hydrogel exhibited no noticeable photothermal property even after 6 min of irradiation. Interestingly, the CQDs-loaded hydrogel exhibited a remarkable change of temperature up to 6 min. The GelMA-Y hydrogel exhibited highest degree of surface temperature rise after irradiation for 6 min at 1.0 W cm⁻². Since, the GelMA-Y hydrogel showed exceptional photothermal properties, therefore it was chosen for rest of the experiments. Notably, the GelMA-Y hydrogel displayed temperature stability

even after 3 cycles of heating and cooling (Figure 2c). The higher photothermal performance and stability of the GelMA-Y hydrogel is probably due to the presence of Y-CQDs with large polyaromatic domain, which resulted in greater NIR responsive properties. The photothermal conversion efficiency (PCE) for GelMA, GelMA-G, and GelMA-Y was calculated as 4.84%, 22.5%, and 49.52%, respectively (Figure 2d).

Based on the outstanding PCE of the GelMA-Y, we have chosen it for drug loading and release study. The 3D printed GelMA-Y scaffold was loaded with chemotherapeutic drugs (Dox and PTX) and used for photothermal therapy. The digital photographs with corresponding FL images of the drug loaded GelMA-Y scaffolds are shown in Figure 2e. Since both of the drugs used in this study are fluorescent, therefore FL microscopy was used to monitor the loading capability. The Dox-loaded and PTX-loaded GelMA-Y scaffolds appeared red and green under 562 nm excitation, which indicates the successful loading of the drugs. The FE-SEM morphology of the GelMA-Y@Dox and GelMA-Y@PTX also exhibited no noticeable change in the morphology. The distinct porous morphology was observed in both the drug-loaded samples (Figure 2f). The drug loading efficiency for Dox and PTX were calculated as 64.28% and 41.54%, respectively (Figure 2g). The higher Dox loading efficiency is probably due to the greater interaction and affinity of Dox with CQDs and/or polymer matrix, since Dox is a hydrophilic drug.

NIR irradiation often leads to the formation of intracellular reactive oxygen species (ROS) owing to the hyperthermia-induced cell damage.^[34] Using the electron paramagnetic resonance (EPR) spectroscopy, we examined the ROS with or without NIR light irradiation, and the result is shown in Figure 2h. The 2,2,6,6-tetramethylpiperidine-1-oxyl (TEMPO) was used as spin trapping agent for ROS experiment. The findings show that the pure TEMPO and GelMA-Y@Dox had no apparent signals for any radical. Surprisingly, the three distinct peak at 1:1:1 intensity ratio was observed between 334 to 340 G after irradiation with NIR light for 6 min, suggesting the presence of single oxygen radicals (¹O₂) as reported in the previous literature.^[34a] The single oxygen generation through GelMA-Y@Dox was probably due to the conversion of ³O₂ → ¹O₂ (type II energy transfer mechanism) in the presence of molecular oxygen. The Therefore, we anticipated that the GelMA-Y@Dox scaffold alone had no capability to produce ROS but produced significant amount of ¹O₂ radical upon NIR irradiation, which could be utilized for hyperthermia-triggered osteosarcoma therapy.

Next, we evaluated the in vitro Dox release study in various pH buffer (pH 6.5 and 7.4) to examine the effect of NIR exposure on release behavior of Dox. The Dox was judiciously chosen owing to its greater loading efficiency. Figure 2i depicts the Dox release profile from the GelMA-Y scaffold with or without NIR irradiation as a function of time. It was interesting to note that, the Dox release profile was nearly similar at both pH in the absence of NIR light. Notably, the release profile of Dox was found higher after periodic NIR light treatment. At pH 7.4, only 23% of Dox was released at 24 h after NIR treatment. However, at pH 6.5, around 38.5% Dox was released after 24 h of incubation under NIR light irradiation. This suggest that NIR irradiation and local hyperthermia owing the presence of Y-CQDs were responsible for the fast release of Dox. Moreover, after 7 d, a slow or sustained release of Dox was noticed in both the groups. This was

Table 1. Doxorubicin release kinetic parameters used in this study (NIR, near-infrared).

Experimental condition	Higuchi model		Korsmeyer-Peppas model	
	pH 6.5	pH 7.4	pH 6.5	pH 7.4
Scaffold + NIR	$n = 1.37$ $R^2 = 0.98021$	$n = 3.23$ $R^2 = 0.99307$	$n = 0.20$ $R^2 = 0.99594$	$n = 0.24$ $R^2 = 0.98937$
Scaffold - NIR	$n = 2.06$ $R^2 = 0.99121$	$n = 2.53$ $R^2 = 0.98901$	$n = 0.37$ $R^2 = 0.99417$	$n = 0.41$ $R^2 = 0.98709$

probably due to the thermal response, scaffold degradation, and concentration-dependent diffusion of Dox in the buffer media.

To gain an insight about the diffusion kinetics, various mathematical models have been employed to understand the effect of nanofiller on drug diffusion.^[26] In this study, we used Higuchi and Korsmeyer-Peppas model to fit the experimental data. For a certain amount of drug (Q) released in specific time (t), the release kinetics can be explained by following equations:

$$Q = k \times t^{1/2} \quad (1)$$

$$\frac{Q}{Q_0} = k \times t^n \quad (2)$$

where, k and n indicate the release constant and release exponent of the respective drug. The Q_0 is the initial amount of drug in the polymer scaffold. The Higuchi model (Equation 1) explains a diffusion process according to the Fick's law where the drug is homogeneously dispersed in the polymer matrix. Conversely, the Korsmeyer-Peppas model (Equation 2) explains drug release profile with a combination of simple drug diffusion (Fickian diffusion) and polymer-induced drug release (non-Fickian, controlled by the polymer chain where the drug is tightly packed in the polymer chain). In this study, we used both the models to predict the diffusion phenomenon of the Dox. The fitting data and its values are listed in **Table 1**. The best fitted release profile was chosen based on the highest correlation coefficient (Pearson's R^2 value) and release exponent (n). As shown in Figure 2k, the Dox release profile was best fitted to Korsmeyer-Peppas model with higher R^2 value for both pH 6.5 and 7.4. However, the Higuchi model doesn't correspond to best fitting owing to the higher value of n ($n > 0.49$) (Figure 2j). The value of n according to Korsmeyer-Peppas model for pH 6.5 and pH 7.4 were calculated to be 0.2 and 0.24, respectively. It is well-known that a value of $n < 0.49$ indicates the Fickian type diffusion and $n > 0.49$ correspond to the anomalous or non-Fickian type diffusion.^[26,35] Thus, both the samples (pH 6.5 and 7.4) after NIR irradiation exhibited the non-Fickian type diffusion, where the CQDs-embedded GelMA matrix controlled the release of the Dox via phototherapy. The hyperthermia effect induced the GelMA matrix to shrink and release the drug molecule in the PBS buffer. This kind of drug release phenomenon is suitable for delivery of chemotherapeutic drugs for anti-infection therapy.^[34b, 36]

Based on excellent drug delivery property of the GelMA-Y scaffold, we selected the GelMA-Y@Dox scaffold for in vitro anti-osteosarcoma study. Since the tumor cell pH is slightly acidic than the physiological pH,^[34b] therefore, we assumed that the GelMA-Y scaffold can effectively delivery the Dox at pH 6.5

under NIR light irradiation. The MG-63 cells were incubated with GelMA-Y@Dox scaffold and irradiated with 1 W cm^{-2} NIR light (808 nm) for 6 min. After 24 h, the viability of the MG-63 cells was assessed using Live/Dead and WST-8 assay. The cells growing on TCPS (2D culture) were taken as negative control. The plates with pure GelMA, GelMA-G, and GelMA-Y were taken as positive control-1 group. The cells cultured with GelMA-Y@Dox but no NIR treatment was taken as positive control group-2. As shown in Figure 2l, the 2D culture group exhibited healthy cells after 24 h of culture, indicated by green (live) color. The cells growing on GelMA, GelMA-G, and GelMA-Y scaffold also appeared to be live. Interestingly, the MG-63 cells growing on GelMA-Y@Dox scaffold showed decreased viability, indicated by the greater number of dead (red) and a few number of live cells (green). Besides, the GelMA-Y@Dox + laser group exhibited higher number of dead cells (red), compared to GelMA-Y@Dox (-laser) or other groups, suggesting that NIR treatment facilitated the sustained release of Dox. A similar kind of result was also observed in the WST-1 assay. Without Dox, the MG-63 viability was significantly increased (144% than control), which is comparable to the proliferation rate of hDFs (Figure 2m). However, after NIR irradiation, the viability was decreased by $\approx 70\%$ compared to the control, which was in agreement with the Live/Dead assay. The primary cause of massive cell death was due to the controlled release of Dox to the MG-63 cells and the hyperthermia-triggered ROS amplification, a common phenomenon of phototherapy.^[37] Therefore, we anticipated that the 3D printed GelMA-Y scaffold is a smart delivery vehicle, where the controlled photothermal property of Y-CQDs can be utilized for sustained release of water-soluble chemotherapeutic drugs, such as Doxorubicin. Figure 2n depicts an overview of the NIR-triggered drug delivery and subsequent phototherapy for ant-osteosarcoma therapy.

2.4. Macrophage Phenotyping and Osteoimmunomodulation Study

Macrophage cells play crucial role osteogenesis and angiogenesis owing to their phenotypic plasticity via secreting various inflammatory factors during early bone and blood vessel formation.^[38] Compared to the M1 macrophages, the M2 polarized macrophages exhibited higher efficacy of bone healing via paracrine signaling of various growth factors and cytokines.^[39] Figure 3a represents an overview of the 3D printed scaffold-assisted macrophage polarization and osseointegration process for bone regeneration. In this study, the fabricated scaffolds (GelMA, GelMA-G, and GelMA-Y) exhibited better proliferation and M2 polarization of the Raw 264.7 cells. As shown in Figure 3b, the Raw 264.7 cells grew properly onto the 3D printed scaffolds after 24 h of incubation. The Raw 264.7 cells appeared to be in cluster and tend to form spheroidal morphology in all the fabricated samples. Interestingly, the average number of cell mass and size was increased in the presence of Y-CQDs containing scaffold than other groups (Figure 3c,d). GelMA hydrogels have been shown previously to enhance the macrophage viability and polarization through various signaling pathways. To examine the actin morphology and macrophage differentiation, we further cultured the Raw 264.7 cells in the scaffold leaching media. As shown in Figure 3, the Raw 264.7 cells differentiated into

macrophage (M0) phenotype in the presence of pure GelMA scaffolds, which is characterized by the extensive branching of the F-actin filaments. The control Raw 264.7 cells exhibited reduced branching pattern with round morphology indicating the undifferentiated monocytes. Notably, the Raw 264.7 cells displayed flattened and dumbbell-shaped morphology without any branches in the presence of GelMA-G and GelMA-Y scaffolds, indicating the M2 polarized macrophages. The presence of CQDs in the GelMA scaffold affected the macrophage differentiation and is further confirmed by optical microscopy, fluorescence activated cell sorting (FACS), immunocytochemistry (ICC), and real-time PCR (qRT-PCR) analysis. The results showed that the Raw 264.7 cells exhibited typical flat morphology in the presence of GelMA-G and GelMA-Y scaffolds (M2 morphology) after 48 h of culture (Figure 3f). However, the cells growing on pure GelMA scaffold exhibited nearly round and/or branched morphology (M1 phenotype) with less number of M2 polarized cells. The average length of the macrophages was found higher ($\approx 114 \pm 10.8 \mu\text{m}$) in the presence of GelMA-Y scaffolds than other groups (Figure 3g), suggesting that Y-CQDs had superior inducing effect on monocytes towards M2 polarization.

The differentiated macrophage (M1 or M2) expresses a variety of surface or cellular markers with various kinds of cytokines and chemokines.^[40] As shown in Figure 3h, the Raw 264.7 cells exhibited positive for CD163 (M2 marker, 38.64%) than NOS2 (M1 marker, 8.94%) in the presence of GelMA-Y scaffolds. In contrast, only 7.59% cells were found positive for CD163 and around 12.96% cells were found positive for NOS2, indicating the polarization towards M1 axis. To verify the intracellular localization of NOS2 and CD163, we performed the ICC of Raw 264.7 cells after 24 h of incubation (Figure 3i). The results indicate that Raw 264.7 cells were highly positive for NOS2 marker and negative for CD163 marker in the presence of GelMA. Conversely, the GelMA-Y grown cells were found highly positive for CD163 marker than NOS2, indicating the polarization towards M2 axis. These results confirmed that the pure GelMA scaffolds had less ability to differentiate the Raw 264.7 cells towards M2 phenotype, whereas the addition of Y-CQDs accelerated the Raw 264.7 cells towards M2 phenotype with greater number. The qRT-PCR results showed similar trend as of morphometric observations. As shown in Figure 3j, the Raw 264.7 cells displayed a downregulation in *TNF- α* and *IL-1 β* expression (pro-inflammatory markers), while showed an upregulation of *IL-4* and *IL-10* genes (anti-inflammatory markers) in the presence of GelMA-Y scaffolds. Similarly, the pure GelMA displayed an upregulation of *TNF- α* and *IL-1 β* genes with significantly less expression of *IL-10* marker. These results suggest that the fabricated GelMA-Y scaffold is non-toxic to Raw 264.7 cells, promoted growth, and differentiated into M2 phenotype which will be beneficial for osteoimmunomodulation and improving bone regeneration.

2.5. 3D Printed GelMA-CQDs Scaffold Promoted In Vitro Angiogenic and Osteogenic Capabilities of hBMSCs

Being a part of the hematopoietic lineage, the hBMSCs have the capability to differentiate into angiogenic and osteogenic lineages.^[41] A smart tissue-engineered scaffold that has the property to induce both angiogenesis and osteogenesis is highly

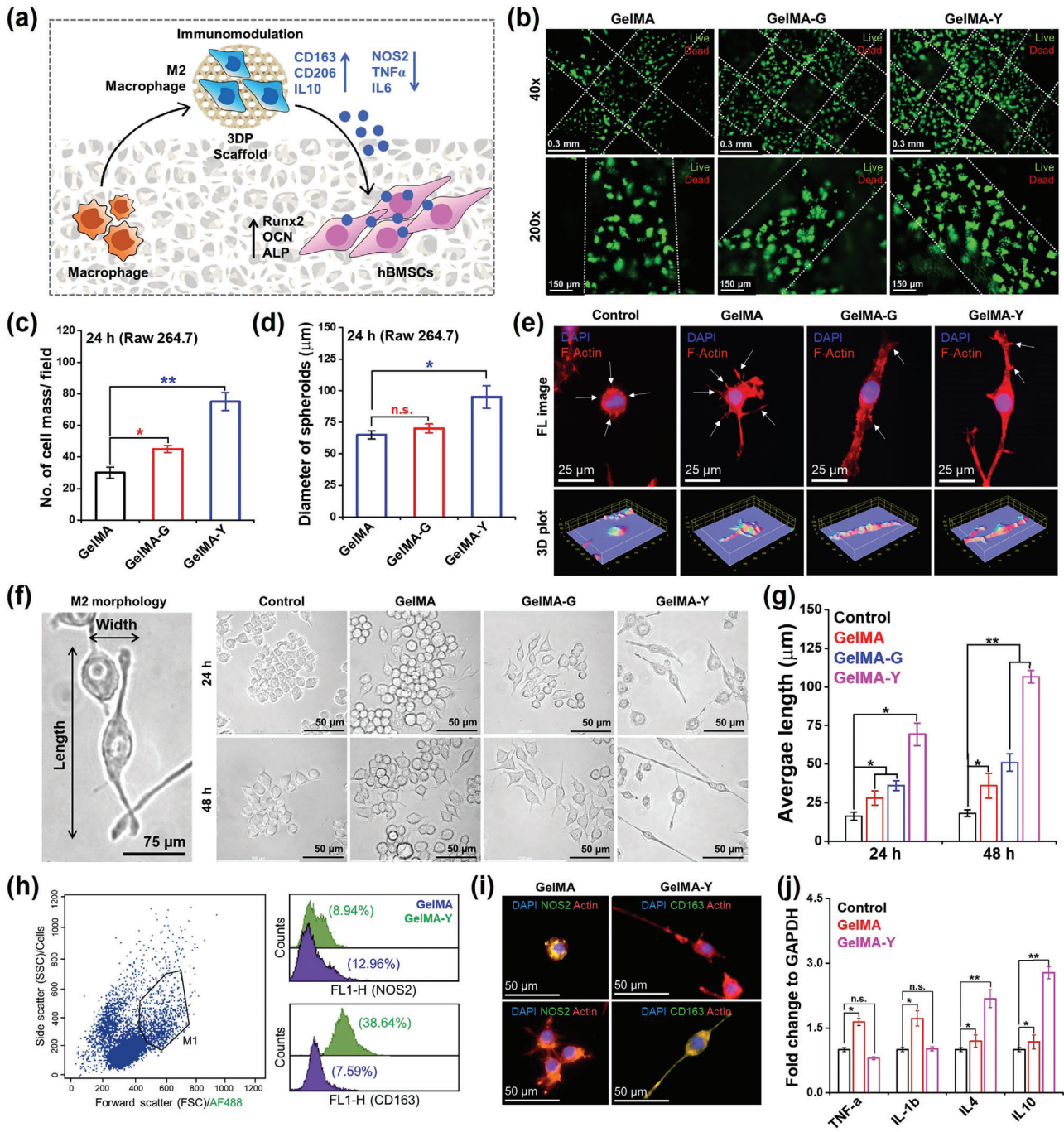


Figure 3. GelMA-CQDs scaffold enhanced macrophage viability and promoted M2 polarization in vitro. a) Schematic diagram for the M2 polarization and osteo-immunomodulation. b) FL microscopy images of the Raw 264.7 cells showing the Live/Dead morphology in the presence of GelMA-CQDs scaffolds after 24 h of culture. Dotted line indicates the printed strands. d,e) Quantification of the average cell mass and spheroids growing onto the scaffolds. e) Representative FL images of Raw 264.7 cells showing the actin distribution and branching pattern. f) Optical micrographs of the Raw 264.7 cells showing the M2 polarization in the presence of various scaffolds. g) The average length (long axis) of the M2 macrophages in various treatment groups after 24 and 48 h of incubation. h) Flow cytometric analysis of Raw 264.7 cells in the presence of 3D scaffolds for NOS2 (M1) and CD163 (M2) markers. i) Immunocytochemical staining of NOS2 and CD163 markers after 24 h of culture. j) qRT-PCR results showing the expression of *Tnf- α* , *IL-1 β* , *IL-4*, and *IL-10* after 24 h of culture. Scale bars: 50, 75, 150 μ m and 0.2 mm. Data are reported as mean \pm s.d. ($n = 3$), * $p < 0.05$ and ** $p < 0.01$.

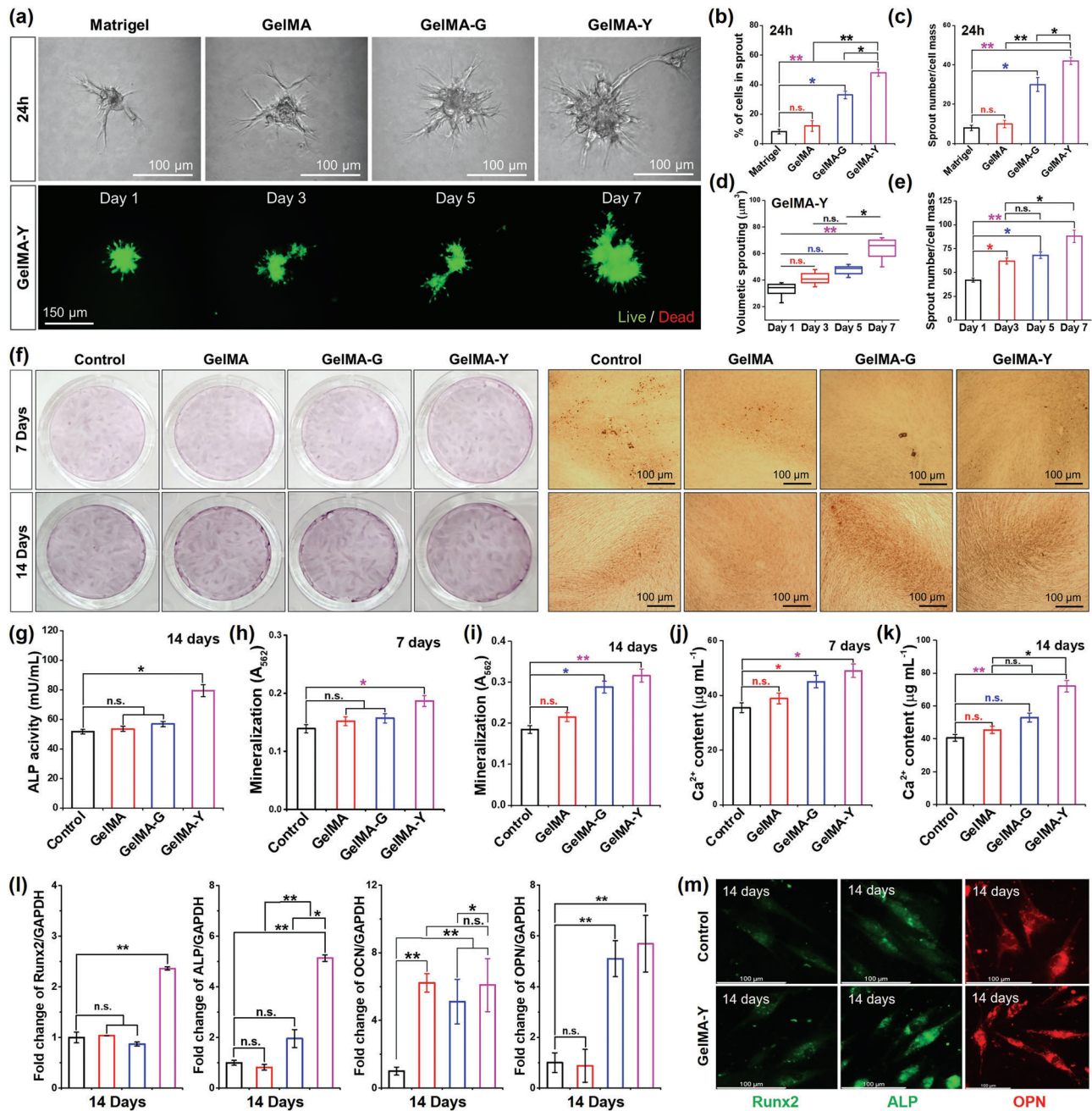


Figure 4. In vitro angiogenic and osteogenic potential of hBMSCs. a) Representative bright field and FL images of hBMSCs showing the angiogenic sprouts in the presence of bioprinted constructs. b,c) Quantification of sprout number inside the bioprinted constructs. d,e) Quantification of the Live/Dead assay of the angiogenic sprouts. f) Representative ARS staining with corresponding microscopic images showing the presence of ARS⁺ cells in the presence of fabricated scaffolds. g) ALP activity of the hBMSCs in the presence of fabricated scaffolds after 14 d of incubation. h,i) The ARS quantification test of the hBMSCs after 7 and 14 d of incubation. j,k) Quantification data of the calcium content assay. l) qRT-PCR analysis for the osteogenesis-related gene markers after 14 d of incubation. m) FL images of the hBMSCs after staining with immunogenic markers: Runx2 (green), ALP (green), and OPN (red). Scale bar: 100 and 150 μm. Data are reported as mean ± s.d. (n = 3), *p < 0.05 and **p < 0.01.

desired in orthopedics, especially for traumatic injury repair.^[42] For the angiogenesis study, the hBMSCs (2.5×10^4 cells) were bioprinted using GelMA-CQDs hydrogel and incubated with Opti-MEM media without VEGF supplement for 24 h. The Matrigel coated plates were considered as control. After 24 h, the bioprinted constructs were photographed and the angiogenic po-

tential was measured. As shown in **Figure 4a**, top, the hBMSCs were appeared to form several branched networks. Among the various formulations, the GelMA-Y hydrogel-laden hBMSCs exhibited higher number of sprouts formation compared to other groups (**Figure 4a**, bottom). Moreover, the % of cells, sprout number, and average sprout volume were significantly elevated

in the presence of GelMA-Y hydrogel (Figure 4b–e), suggesting that GelMA-Y hydrogel had better angiogenic induction property owing to the presence of bioactive Y-CQDs. Next, we evaluated the osteogenic potential of the fabricated hydrogel scaffolds in terms of ARS staining, ALP activity, calcium content assay, and fluorescent marker staining, respectively. As indicated in Figure 4f, the ARS stained plates exhibited no significant difference even after 14 d of incubation. However, the optical micrographs displayed a significant change in mineral deposition. The GelMA-Y treated hBMSCs exhibited higher mineral induction efficiency after 14 d of osteo-induction. This was also reflected in the ALP activity. Compared to the control, the GelMA-Y group displayed higher ALP activity ($*p < 0.05$) after 14 d of treatment (Figure 4g). The quantification test of mineralization test was also found higher in the presence of GelMA-Y (Figure 4h,i). The osteoblast cells have the ability to produce intracellular bone apatite and the excess amount of apatite is secreted in the form of inorganic Ca^{2+} or PO_4^{2-} .^[43] Based on the above-mentioned results we investigated the Ca^{2+} content from the cell culture soup after 14 d of osteo-induction and the results are given in Figure 4j,k. It is interesting to note that the 3D printed scaffolds raised the extracellular Ca^{2+} level than the control group. Among the treatment groups, the GelMA-Y scaffold promoted higher Ca^{2+} production ($**p < 0.01$) in hBMSCs compared to the pure GelMA and GelMA-G scaffolds. In light of this finding, we further investigated the expression of various osteogenic gene markers after 14 d of osteoinduction. As shown in Figure 4l, the expression of early gene markers (*Runx2* and *ALP*) was significantly ($**p < 0.01$) increased after treatment with GelMA-Y scaffold than control, suggesting that the supplement of GelMA-CQD had a positive role in osteogenesis. Similarly, the expression of late gene markers (*OCN* and *OPN*) was also found higher ($**p < 0.01$) in the presence of GelMA-Y scaffold. To support the above-mentioned findings, we also investigated the levels of osteogenic protein markers (*Runx2*, *ALP*, *OCN*, and *OPN*) through IF staining (Figure 4m) which indicate that both the control and GelMA-Y scaffolds have positive role in osteogenic differentiation of hBMSCs. The quantification data of IF staining is given in Figure S9 (Supporting Information). Taken together, our results demonstrated that the 3D printed GelMA-CQD hydrogel had better angiogenic and osteogenic induction property, which could be utilized for developing smart orthopedic grafts.

2.6. Immunomodulation-Assisted Enhanced Osseointegration

Bone is a complex tissue which comprises a variety of cell populations, such as osteoblast, osteoclast, osteocyte, immune cells, and blood cells. After implantation of a scaffold, the new bone formation profoundly affected by the continuous cross-talk between bone and immune cells.^[44] Accordingly, the osteo-immunomodulatory effects of the fabricated scaffolds were evaluated in the presence of macrophage conditioned media (M-CM). As discussed earlier, the GelMA-Y scaffolds had better anti-inflammatory function; therefore, the GelMA-Y scaffold was chosen for osteo-immunomodulatory experiment. A schematic design of the M-CM preparation and immunomodulation study is shown in Figure S10 (Supporting Information). The immunomodulatory effects of the M-CM on hBMSCs is evaluated

through ARS staining (for 2D and 3D culture), H&E (for 3D culture) and Massion's Trichrome staining (for 3D culture), respectively. As shown in Figure 5a, the M-CM(GY) had better osteo-immunomodulatory effect as documented by ARS staining after 7 d. The intense and red color of the mineralized nodule signifies the induction of osteogenesis. The percentage of ARS⁺ area was also increased significantly ($\text{ARS}_{\text{M-CM@Ctrl}} = 22\% \rightarrow \text{ARS}_{\text{M-CM@GY}} = 41.6\%$, $*p < 0.05$) after treatment with M-CM (GY) (Figure 5b). A similar kind of trend was observed after 14 d of osteogenic induction, where more intense nodule formation was observed in hBMSCs following M-CM (GY) treatment (Figure 5c). The ARS starting area for M-CM (Ctrl) and M-CM (GY) were calculated as 42% and 73%, respectively (Figure 5d). The 3D cell culture also exhibited similar trend. For example, the ARS staining of hBMSC spheroids exhibited highly mineralized and intense red color after incubation with M-CM (GY) than M-CM (Ctrl) after 14 d of osteoinduction (Figure 5e). The quantity of nodule was found greater (3.2-fold) at 14 days in the presence of M-CM (GY) as shown in Figure 5f. Therefore, we evaluated the H&E and Trichrome staining to evaluate the growth of the whole spheroids. The results are displayed in Figure 5g,h. It is interesting to note that both the groups exhibited better growth and morphology after 14 d of immune-modulation. The collagen content (Trichrome staining) of the spheroid was significantly enhanced following treatment with M-CM (GY). The IF staining (Figure 5i) was further performed to examine the expression of *Runx2* and *OCN* markers. In 2D culture system, both the M-CM (Ctrl) and M-CM (GY)-treated plates exhibited positive for *Runx2* and *OCN* after 14 d of treatment. Interestingly, the expression of *Runx2* and *OCN* markers were significantly upregulated after M-CM (GY) treatment (Figure S11, Supporting Information) as per the quantitative evaluation. Collectively, our results demonstrated that the anti-inflammatory macrophages regulate the hBMSC differentiation via immune cross-talk and the 3D culture system depicted better osteogenesis model in this study. Thus, we hypothesized that a combination of M-CM (GY) with OIM may induce the osteogenic potential of hBMSCs towards bone healing.

2.7. 3D Printed GelMA-Y Scaffold Promotes Bone Regeneration In Vivo

Vascularized bone regeneration refers to the development of neo-angiogenesis which indirectly facilitate the new bone formation via signaling through endothelial cells to osteoblast cells. The angiogenic cells secrete the VEGF, FGF-2, PDGF, and IGF, which contributes to osteoblast migration, osteocyte maturation, and calcified bone matrix formation [99]. To investigate the in vivo bone regeneration potential, we have randomly divided the rats into three groups: 1) -ve control group (no scaffold treatment; $n = 3$), 2) +ve control group (pure GelMA scaffold; $n = 3$), and 3) experimental group (GelMA-Y scaffold; $n = 3$), respectively. The experimental timeline and digital photographs of the surgical procedure are shown in Figure 6a. After 8 weeks' post-implantation, the rat skull was harvested, decalcified, and evaluated using micro-computed tomography (μCT), followed by H&E staining. As shown in Figure 6b and Figure S12 (Supporting Information), the GelMA-Y treated groups exhibited significantly ($**p < 0.01$) higher rate of bone regeneration ($\approx 94.25 \pm$

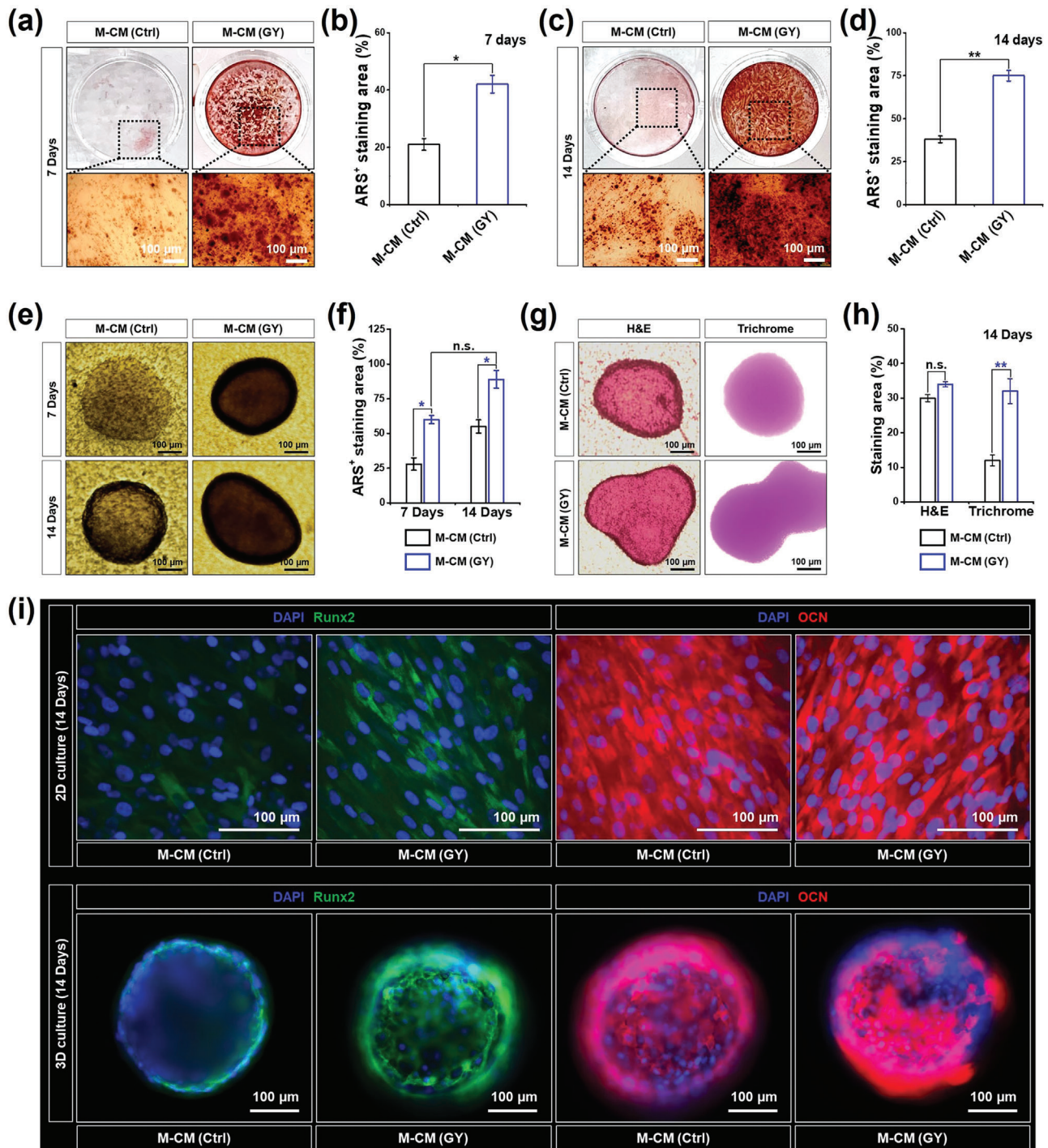


Figure 5. Evaluation of osteo-immunomodulatory effects of macrophage-conditioned media (M-CM) on hBMSCs. a,c) Representative ARS stained plates with optical micrographs of the 2D culture of hBMSCs after 7 and 14 d of incubation. b,d) The ARS quantification of 2D culture system. e) ARS staining plates with optical micrographs of hBMSCs in 3D culture after 14 d of incubation. f) ARS quantification of 3D culture system. g,h) Representative H&E and Massion's Trichrome staining of hBMSC spheroids with corresponding quantification data after 14 d of osteo-immunomodulation. i) FL microscopy images of hBMSCs in 2D and 3D culture showing the expression of Runx2 and OCN marker after 14 d of culture. Scale bar: Scale bars: 100 μ m. Data are reported as mean \pm s.d. ($n = 3$), * $p < 0.05$ and ** $p < 0.01$.

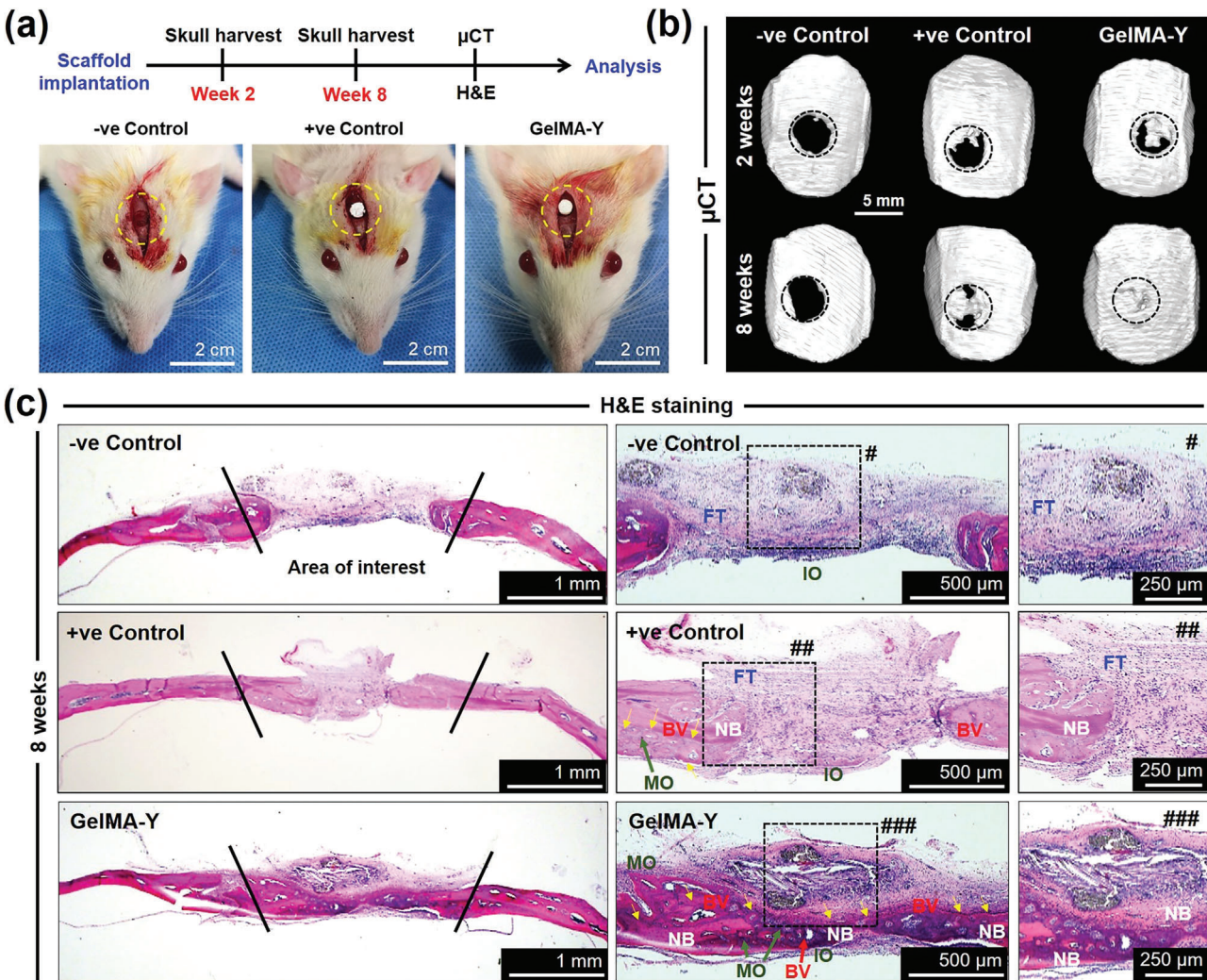


Figure 6. In vivo bone regeneration potential of the 3D printed scaffolds. a) The experimental timeline, digital photographs of the surgical procedure in rats, and scaffold implantation procedure used in this study. The yellow dotted circle indicates the area of interest. b) Representative micro-computed tomography (μ CT) images of the decalcified rat skull showing the new bone formation (black dotted circle). c) Representative hematoxylin and eosin (H&E) staining images of the calvaria defect region showing the vascularized bone regeneration. Rats without any scaffold treatment were considered as -ve control. Rats with GelMA and GelMA-Y scaffold was considered as +ve control and experimental group. The black line indicates the area of interest. The FT, IO, MO, NB, BV denotes fibrous tissue, immature osteocyte, mature osteocyte, new bone, and blood vessels, respectively. The yellow arrow indicates the presence of osteoblast lining. Scale bar: 250 μ m, 500 μ m, 1 mm, and 2 cm.

0.82%) and bone mineralization ($BMD_{\text{GelMA-Y}} = 0.48 \text{ g cm}^{-3}$), compared to the +ve ($BMD = 0.25 \text{ g cm}^{-3}$) and -ve control ($BMD = 0.18 \text{ g cm}^{-3}$) groups. The gross morphology of the μ CT images showed that the regenerative potential of the GelMA-Y treated scaffold was undoubtedly better than the +ve control groups, which is not comparable to the -ve control group where relatively poor regeneration potential was observed after 8 weeks of treatment. These results demonstrated that the GelMA scaffold alone indicated the cortical bone formation, which was significantly increased after addition of Y-CQDs (= GelMA-Y scaffold). The entire defect area was found to be covered with new bone in case of GelMA-Y scaffold suggest that the CQDs incorporation had positive role in bone formation. To gain an insight into the vascularized bone formation, we performed the H&E staining and the results are shown in Figure 6c. In the -

ve control group, the poor cortical bone formation was characterized by the presence of huge fibrous tissue (FT) with some immature osteocytes (IO). Concurrently, the +ve control group exhibited greater new bone regeneration potential which was characterized by the presence of osteoblasts, mature osteocytes (MO), and a few blood vessels (BV) in the defect area. Surprisingly, the GelMA-Y groups showed a huge difference from the +ve and -ve control groups. The GelMA-Y treated group exhibited robust bone regeneration, characterized by the formation of many BVs, osteoblasts, MO, and a heavily calcified bone matrix. A prominent osteoblast lining was observed in the defect area with diffused blood vessel, suggesting that the new bone formation was accomplished with extensive vascularization in the GelMA-Y treated group. Therefore, we anticipate that the 3D bioprinted and chemoprotective GelMA-Y scaffold not only promoted bone

regeneration but also enhanced the vascularization during bone remodeling.

3. Conclusion

In conclusion, this study demonstrates the fabrication of a CQDs engineered hydrogel inks with both osteogenic and immunomodulatory properties for improving osteo-immunity. Moreover, the outstanding photothermal and light-induced controlled drug release mechanism provides a new functional strategy for osteosarcoma eradication and simultaneous bone regeneration within a single hydrogel. The developed bioink is highly shear-thinning and friendly to the hBMSCs and hECs, and induced angiogenesis owing to the biocompatible and proliferative nature of the CQDs. The composite bioink helped to polarize the Raw 264.7 cells towards M2 phenotype which facilitates the osteogenic differentiation of hBMSCs. The in vivo results suggest that the as-fabricated GelMA-CQD scaffold had positive role in new bone formation and provided sufficient mechanical stability during osteogenic differentiation. Overall, this study highlights a new strategy of bone healing and regeneration using nano-carbon materials via immunopolarization, tumor apoptosis, sustained drug delivery, and osteo-immunity for better osseointegration.

4. Experimental Section

Detailed methods are given in the Supporting Information file.

Materials and Instruments: Gelatin type B from porcine skin (purity >98%), 1, 3, 5-trihydroxybenzene (phloroglucinol, C₇H₆O₄), sulfuric acid (H₂SO₄), methacrylic anhydride (purity >94%), and lithium phenyl-2,4,6-trimethylbenzoylphosphinate (LAP) were obtained from Sigma-Aldrich, USA. All the materials were used as received unless stated elsewhere. Milli-Q water (18.2 MΩ cm⁻¹ @25 °C) was used for the synthesis of CQDs and other polymer materials. HR-TEM (JEM 3010, Jeol, Japan) and FE-SEM (Jeol, Japan) were used for evaluating the morphology of the CQDs and polymer scaffolds. The UV-Vis spectrophotometer (Varian Cary 100, Nevada, USA) and PL spectrometer (Quanta Master, photon Technology International, New Jersey, USA) were used to evaluate the luminescent properties of the CQDs. FT-IR spectrophotometer (Bruker Vertex 70, Bruker, Massachusetts, USA) was used to measure the functional properties and chemical interaction of the CQDs and polymer scaffolds. The surface functional group and interaction of the CQDs was investigated using X-ray photoelectron spectroscopy (XPS) using an X-ray source with a twin-anode (Al-Kα, hν = 1486.6 eV) gun and a monochromatic gun. The structural features of the CQDs was evaluated through an X-ray diffractometer (XRD, Smart-Lab, Rigaku, Japan) equipped with a 4 kW X-ray generator and a D/teX Ultra 250 detector system. The Raman spectra was recorded using a micro-Raman spectrophotometer (ANDOR Monora500i, Oxford Instruments, UK) with an excitation laser of 633 nm.

3D Bioprinting and Cell Culture: Cellink Bio-X (Cellink Corporation, Sweden) 3D printer was used for bioprinting. Single-nozzle hydrogel cartridge was used to fabricate the constructs. The cell-laden bioinks were fabricated by mixing the appropriate amount of cells (hBMSCs or hECs) and GelMA-CQD hydrogel solution (1:1 ratio). The 3D bioprinted constructs were photo-crosslinked using 365 nm UV light. The bioprinted constructs were cultured in DMEM media supplemented with 10% FBS and 1% antibiotics. The old media was replaced every another day.

Ethical Statement: All the animal experiments were conducted according to the guidelines of IACUC (Permission No. KQYY-201912-003) of Capital Medical University, Beijing.

Statistical Analysis: The statistical analysis was performed using Origin Pro v9.0 software (Origin Lab, USA). One-way analysis of variance

(ANOVA) test was conducted to determine the significant difference between control and treated groups. Data are reported as mean ± s.d. of triplicated (n = 3) experiments, statistical significance at *p < 0.05 and **p < 0.01.

Supporting Information

Supporting Information is available from the Wiley Online Library or from the author.

Acknowledgements

S.D.D., K.G., and J.H. contributed equally to this work. This work was supported by the Basic Science Research Program' through the "National Research Foundation of Korea (NRF)" funded by the Ministry of Education (2018R1A1A1A03025582, 2019R1D1A3A03103828, and 2022R111A3063302).

Conflict of Interest

The authors declare no conflict of interest.

Data Availability Statement

The data that support the findings of this study are available from the corresponding author upon reasonable request.

Keywords

anti-inflammatory, multifunctional hydrogel, osteoimmunity, polyphenolic carbon quantum dots, tumor ablation

Received: March 8, 2023

Revised: April 12, 2023

Published online:

- [1] a) H. Xue, Z. Zhang, Z. Lin, J. Su, A. C. Panayi, Y. Xiong, L. Hu, Y. Hu, L. Chen, C. Yan, *Bioact. Mater.* **2022**, *18*, 552; b) Y. Zhu, B. Kong, R. Liu, Y. Zhao, *Smart Med.* **2022**, *1*, e20220006; c) Z. Luo, J. Che, L. Sun, L. Yang, Y. Zu, H. Wang, Y. Zhao, *Eng. Regener.* **2021**, *2*, 257.
- [2] B. N. Brown, B. D. Ratner, S. B. Goodman, S. Amar, S. F. Badylak, *Biomaterials* **2012**, *33*, 3792.
- [3] a) A. R. D. Reeves, K. L. Spiller, D. O. Freytes, G. Vunjak-Novakovic, D. L. Kaplan, *Biomaterials* **2015**, *73*, 272; b) J. Ye, C. Xie, C. Wang, J. Huang, Z. Yin, B. C. Heng, X. Chen, W. Shen, *Bioact. Mater.* **2021**, *6*, 4096.
- [4] A. Mantovani, A. Sica, S. Sozzani, P. Allavena, A. Vecchi, M. Locati, *Trends Immunol.* **2004**, *25*, 677.
- [5] a) A. K. Gaharwar, I. Singh, A. Khademhosseini, *Nat. Rev. Mater.* **2020**, *5*, 686; b) Z. Tu, Y. Zhong, H. Hu, D. Shao, R. Haag, M. Schirner, J. Lee, B. Sullenger, K. W. Leong, *Nat. Rev. Mater.* **2022**, *7*, 557.
- [6] a) F. Loi, L. A. Córdova, J. Pajarinen, T.-H. Lin, Z. Yao, S. B. Goodman, *Bone* **2016**, *86*, 119; b) Y. Gao, Q. Ma, *Smart Med.* **2022**, *1*, 1.
- [7] Z. Fu, Y. Zhuang, J. Cui, R. Sheng, H. Tomás, J. Rodrigues, B. Zhao, X. Wang, K. Lin, *Eng. Regener.* **2022**, *3*, 163.
- [8] H. Xue, L. Hu, Y. Xiong, X. Zhu, C. Wei, F. Cao, W. Zhou, Y. Sun, Y. Endo, M. Liu, Y. Liu, J. Liu, A. Abududilibaier, L. Chen, C. Yan, B. Mi, G. Liu, *Carbohydr. Polym.* **2019**, *226*, 115302.

- [9] R. C. H. Gresham, C. S. Bahney, J. K. Leach, *Bioact. Mater.* **2021**, 6, 1945.
- [10] Y. Niu, L. Wang, N. Yu, P. Xing, Z. Wang, Z. Zhong, Y. Feng, L. Dong, C. Wang, *Acta Biomater.* **2020**, 111, 153.
- [11] a) A. P. Kusumbe, S. K. Ramasamy, R. H. Adams, *Nature* **2014**, 507, 323; b) N. Komatsu, H. Takayanagi, *Nat. Rev. Rheumatol.* **2022**, 18, 1.
- [12] a) M. Zhang, C. Qin, Y. Wang, X. Hu, J. Ma, H. Zhuang, J. Xue, L. Wan, J. Chang, W. Zou, C. Wu, *Addit. Manuf.* **2022**, 54, 102721; b) S. K. Ghorai, A. Dutta, T. Roy, P. Guha Ray, D. Ganguly, M. Ashokkumar, S. Dhara, S. Chattopadhyay, *ACS Appl. Mater. Interfaces* **2022**, 14, 28455.
- [13] a) C. Wang, W. Huang, Y. Zhou, L. He, Z. He, Z. Chen, X. He, S. Tian, J. Liao, B. Lu, Y. Wei, M. Wang, *Bioact. Mater.* **2020**, 5, 82; b) Y. Chen, L. Chen, Y. Wang, K. Lin, J. Liu, *Composites, Part B* **2022**, 230, 109550.
- [14] a) H. Sun, C. Zhang, B. Zhang, P. Song, X. Xu, X. Gui, X. Chen, G. Lu, X. Li, J. Liang, J. Sun, Q. Jiang, C. Zhou, Y. Fan, X. Zhou, X. Zhang, *Chem. Eng. J.* **2022**, 427, 130961; b) M. Vallet-Regí, E. Ruiz-Hernández, *Adv. Mater.* **2011**, 23, 5177.
- [15] a) Q. Chen, X. Zhao, W. Lai, Z. Li, D. You, Z. Yu, W. Li, X. Wang, *Surf. Coat. Technol.* **2022**, 435, 128236; b) Y. Wang, X. Yuan, J. Ye, F. He, *Ceram. Int.* **2022**, 48, 28557; c) J. Zhang, D. Tong, H. Song, R. Ruan, Y. Sun, Y. Lin, J. Wang, L. Hou, J. Dai, J. Ding, H. Yang, *Adv. Mater.* **2022**, 34, 2202044.
- [16] S. D. Dutta, J. Hexiu, D. K. Patel, K. Ganguly, K.-T. Lim, *Int. J. Biol. Macromol.* **2021**, 167, 644.
- [17] a) S. D. Dutta, K. Ganguly, A. Randhawa, T. V. Patil, D. K. Patel, K.-T. Lim, *Biomaterials* **2023**, 294, 121999; b) K. Ganguly, S. D. Dutta, A. Randhawa, D. K. Patel, T. V. Patil, K.-T. Lim, *Adv. Healthcare Mater.* **2023**, 12, 1.
- [18] a) Z. Zhong, X. Wu, Y. Wang, M. Li, Y. Li, X. Liu, X. Zhang, Z. Lan, J. Wang, Y. Du, S. Zhang, *Bioact. Mater.* **2022**, 10, 195; b) A. E. Pazarçeviren, S. Akbaba, Z. Evis, A. E. Tezcaner, *ACS Biomater. Sci. Eng.* **2022**, 8, 3038; c) M. N. Collins, G. Ren, K. Young, S. Pina, R. L. Reis, J. M. Oliveira, *Adv. Funct. Mater.* **2021**, 31, 2010609.
- [19] a) B. Geng, F. Fang, P. Li, S. Xu, D. Pan, Y. Zhang, L. Shen, *Chem. Eng. J.* **2021**, 417, 128125; b) B. Geng, P. Li, F. Fang, W. Shi, J. Glowacki, D. Pan, L. Shen, *Carbon* **2021**, 184, 375; c) M. Majood, P. Garg, R. Chaurasia, A. Agarwal, S. Mohanty, M. Mukherjee, *ACS Omega* **2022**, 7, 28685. d) A. Rafieerad, W. Yan, G. L. Sequiera, N. Sareen, E. Abu-El-Rub, M. Moudgil, S. Dhingra, *Adv. Healthcare Mater.* **2019**, 8, 1900569; e) Z. Wang, H. Yang, Y. Bai, L. Cheng, R. Zhu, *Biomed. Mater.* **2022**, 17, 024101; f) H. Li, D. He, X. Xiao, G. Yu, G. Hu, W. Zhang, X. Wen, Y. Lin, X. Li, H. Lin, *ACS Appl. Mater. Interfaces* **2021**, 13, 25290.
- [20] L. Đorđević, F. Arcudi, M. Cacioppo, M. Prato, *Nat. Nanotechnol.* **2022**, 17, 112.
- [21] M. Moniruzzaman, S. D. Dutta, J. Hexiu, K. Ganguly, K.-T. Lim, J. Kim, *Biomater. Sci.* **2022**, 10, 3527.
- [22] Z. Yuan, X. Yuan, Y. Zhao, Q. Cai, Y. Wang, R. Luo, S. Yu, Y. Wang, J. Han, L. Ge, J. Huang, C. Xiong, *Small* **2021**, 17, 2006596.
- [23] a) W. Xu, B. Z. Molino, F. Cheng, P. J. Molino, Z. Yue, D. Su, X. Wang, S. Willför, C. Xu, G. G. Wallace, *ACS Appl. Mater. Interfaces* **2019**, 11, 8838; b) N. Zandi, B. Dolatyar, R. Lotfi, Y. Shallageh, M. A. Shokrgozar, E. Tamjid, N. Annabi, A. Simchi, *Acta Biomater.* **2021**, 124, 191; c) N. Annabi, D. Rana, E. Shirzaei Sani, R. Portillo-Lara, J. L. Gifford, M. M. Fares, S. M. Mithieux, A. S. Weiss, *Biomaterials* **2017**, 139, 229; d) R. I. R. Ibañez, R. J. F. C. Do Amaral, R. L. Reis, A. P. Marques, C. M. Murphy, F. J. O'Brien, *Polymers* **2021**, 13, 2510.
- [24] K. Ganguly, H. Jin, S. D. Dutta, D. K. Patel, T. V. Patil, K.-T. Lim, *Carbohydr. Polym.* **2022**, 287, 119321.
- [25] H. Kamata, X. Li, U.-I. Chung, T. Sakai, *Adv. Healthcare Mater.* **2015**, 4, 2360.
- [26] E. P. Milan, V. C. A. Martins, M. M. Horn, A. M. G. Plepis, *Carbohydr. Polym.* **2022**, 292, 119647.
- [27] D. Chawla, T. Kaur, A. Joshi, N. Singh, *Int. J. Biol. Macromol.* **2020**, 144, 560.
- [28] C. Ji, A. Khademhosseini, F. Dehghani, *Biomaterials* **2011**, 32, 9719.
- [29] a) H. Cui, W. Zhu, Y. Huang, C. Liu, Z.-X. Yu, M. Nowicki, S. Miao, Y. Cheng, X. Zhou, S.-J. Lee, Y. Zhou, S. Wang, M. Mohiuddin, K. Horvath, L. G. Zhang, *Biofabrication* **2019**, 12, 015004; b) G. Janarthanan, S. Lee, I. Noh, *Adv. Funct. Mater.* **2021**, 31, 2104441; c) S. D. Dutta, J. Bin, K. Ganguly, D. K. Patel, K.-T. Lim, *RSC Adv.* **2021**, 11, 20342.
- [30] S. D. Dutta, K. Ganguly, M.-S. Jeong, D. K. Patel, T. V. Patil, S.-J. Cho, K.-T. Lim, *ACS Appl. Mater. Interfaces* **2022**, 14, 34513.
- [31] a) S. Yi, Q. Liu, Z. Luo, J. J. He, H.-L. Ma, W. Li, D. Wang, C. Zhou, C. E. Garciamendez, L. Hou, J. Zhang, Y. S. Zhang, *Small* **2022**, 18, 2106357; b) Z. Galliger, C. D. Vogt, H. R. Helms, A. Panoskaltis-Mortari, *Macromol. Mater. Eng.* **2022**, 307, 2200196.
- [32] C. Yang, H. Ma, Z. Wang, M. R. Younis, C. Liu, C. Wu, Y. Luo, P. Huang, *Adv. Sci.* **2021**, 8, 2100894.
- [33] X. Wang, T. Li, H. Ma, D. Zhai, C. Jiang, J. Chang, J. Wang, C. Wu, *NPG Asia Mater.* **2017**, 9, e376.
- [34] a) K. Onbasli, M. Erkisa, G. Demirci, A. Muti, E. Ulukaya, A. Senaroglu, H. Yagci Acar, *Biomater. Sci.* **2022**, 10, 3951; b) S. D. Dutta, J. Hexiu, J. Kim, S. Sarkar, J. Mondal, J. M. An, Y.-K. Lee, M. Moniruzzaman, K.-T. Lim, *Biomater. Sci.* **2022**, 10, 1680.
- [35] a) F. Asghari, M. Samiei, K. Adibkia, A. Akbarzadeh, S. Davaran, *Artif. Cells, Nanomed., Biotechnol.* **2017**, 45, 185; b) S. Lei, Y. Gao, J. Li, X. Chen, W. Zhou, J. Wu, P. Ma, K. Men, X. Duan, *J. Controlled Release* **2022**, 344, 97.
- [36] D. K. Patel, S. D. Dutta, K. Ganguly, K.-T. Lim, *Int. J. Biol. Macromol.* **2021**, 170, 178.
- [37] a) Y. Li, G. Bai, S. Zeng, J. Hao, *ACS Appl. Mater. Interfaces* **2019**, 11, 4737; b) X.-L. Hu, N. Kwon, K.-C. Yan, A. C. Sedgwick, G.-R. Chen, X.-P. He, T. D. James, J. Yoon, *Adv. Funct. Mater.* **2020**, 30, 1907906.
- [38] D.-W. Zhao, C. Liu, K.-Q. Zuo, P. Su, L.-B. Li, G.-Y. Xiao, L. Cheng, *Chem. Eng. J.* **2021**, 408, 127362.
- [39] a) S. Wang, F. Wang, X. Zhao, F. Yang, Y. Xu, F. Yan, D. Xia, Y. Liu, *Mater. Des.* **2022**, 217, 110621; b) L. Tan, J. Fu, F. Feng, X. Liu, Z. Cui, B. Li, Y. Han, Y. Zheng, K. W. K. Yeung, Z. Li, S. Zhu, Y. Liang, X. Feng, X. Wang, S. Wu, *Sci. Adv.* **2020**, 6, eaba5723; c) Y. Zhao, L. Bai, Y. Zhang, R. Yao, Y. Sun, R. Hang, X. Chen, H. Wang, X. Yao, Y. Xiao, R. Hang, *Biomaterials* **2022**, 288, 121684.
- [40] W. Ying, P. S. Cheruku, F. W. Bazer, S. H. Safe, B. Zhou, *J. Visualized Exp.* **2013**, 76, 50323.
- [41] J. Chen, L. Deng, C. Porter, G. Alexander, D. Patel, J. Vines, X. Zhang, D. Chasteen-Boyd, H.-J. Sung, Y.-P. Li, *Sci. Rep.* **2018**, 8, e15749.
- [42] K. Yu, Z. Jiang, X. Miao, Z. Yu, X. Du, K. Lai, Y. Wang, G. Yang, *Mol. Ther.* **2022**, 30, 3226.
- [43] S. Boonrungsiman, E. Gentleman, R. Carzaniga, N. D. Evans, D. W. Mccomb, A. E. Porter, M. M. Stevens, *Proc. Natl. Acad. Sci. USA* **2012**, 109, 14170.
- [44] a) T. Wang, J. Bai, M. Lu, C. Huang, D. Geng, G. Chen, L. Wang, J. Qi, W. Cui, L. Deng, *Nat. Commun.* **2022**, 13, e160; b) C. Yang, Z. Zheng, M. R. Younis, C. Dong, Y. Chen, S. Lei, D.-Y. Zhang, J. Wu, X. Wu, J. Lin, X. Wang, P. Huang, *Adv. Funct. Mater.* **2021**, 31, 2101372.